

LiDAR-based Control of Autonomous Rotorcraft for the Inspection of Pier-like Structures

Bruno J. Guerreiro, Carlos Silvestre, Rita Cunha, David Cabecinhas

Abstract—This paper addresses the problem of trajectory tracking control of autonomous rotorcraft in operation scenarios where only relative position measurements obtained from LiDAR sensors are possible. The proposed approach defines an alternative kinematic model, directly based on LiDAR measurements, and uses a trajectory-dependent error space to express the dynamic model of the vehicle. An LPV representation with piecewise affine dependence on the parameters is adopted to describe the error dynamics over a set of predefined operating regions, and a continuous-time \mathcal{H}_2 control problem is solved using LMIs and implemented within the scope of gain-scheduling control theory. The performance of the proposed control method is validated with comprehensive simulation and experimental results, using a mock-up scenario of a pier inspected by a quadrotor.

Index Terms—Trajectory Tracking, Sensor-based Control, LiDAR, Aerial Vehicles.

I. INTRODUCTION

The structural components of large infrastructures are affected in their strength and durability by aging, exposure to aggressive/corrosive environment, and wear & tear, especially in places where construction or maintenance errors occurred [1]. As it is essential to perform regular inspection surveys, the cost and risk reduction stemming from the improved detection and from the replacement of the standard procedures support the widespread adoption of automatic inspection tools in a near future, for which autonomous rotorcraft vehicles are ideal platforms that can be equipped with multiple sensors, such as multi-spectral camera arrays or light detection and ranging (LiDAR) sensors, as in the vehicle depicted in Fig. 1.

The development of trajectory tracking control systems is both a challenge and a fundamental requirement to accomplish high performance autonomous flight near infrastructures, particularly, in the absence of GPS measurements. To address

This work was partially funded by the Macau Science and Technology Development Fund (FDCT), grant FDCT/048/2014/A1, by project MYRG2015-00127-FST of the Univ. of Macau, by the European Union's Horizon 2020 research and innovation programme under grant agreement No 731667 (MULTIDRONE), and by the Portuguese Foundation for Science and Technology (FCT), under projects LARSyS UID/EEA/50009/2013 and LOTUS PTDC/EEI-AUT/5048/2014. The work of B. Guerreiro and R. Cunha were respectively supported by the FCT Post-doc Grant SFRH/BPD/110416/2015 and FCT Investigator Programme IF/00921/2013. This publication reflects the authors' views only. The European Commission and other funding institutions are not responsible for any use that may be made of the information it contains.

B. Guerreiro and R. Cunha are with the Institute for Systems and Robotics (ISR-Lisbon), LARSyS, Instituto Superior Técnico (IST), Universidade de Lisboa, Av. Rovisco Pais 1, 1049 Lisboa, Portugal. (bguerreiro@isr.tecnico.ulisboa.pt and rita@isr.tecnico.ulisboa.pt)

C. Silvestre and D. Cabecinhas are with the Department of Electrical and Computer Engineering, Faculty of Science and Technology, University of Macau, Taipa, Macau, China, and C. Silvestre is also on leave from IST, Portugal. (csilvestre@umac.mo and dcabecinhas@umac.mo)



Fig. 1. Aerial vehicle developed for infrastructure inspection.

the trajectory tracking control problem, several authors have focused on using nonlinear techniques, such as backstepping, feedforward control [2], or model predictive control [3]. An alternative to tackle the design of controllers for vehicles with complex nonlinear dynamic models, is to resort to gain-scheduling control theory [4], where a simple controller is designed for each region of operation, and an overall stabilizing controller is obtained by switching between them. In combination with gain-scheduling techniques, linear parameter varying (LPV) models and linear matrix inequalities (LMIs) are frequently used for the design of each controller (see [5] and [6]), which together constitute powerful tools for tackling complex problems. Several examples in the literature attest its level of success, such as [7]–[9].

The use of LiDARs to obtain vehicle localization in GPS-denied environments is by now an ubiquitous and mandatory technology in mobile robots [10]. However, in the field of unmanned aerial vehicles (UAVs) this problem has only been addressed in recent years, for instance in [11] or [12], which either assume that the environment map is known or use computationally demanding simultaneous localization and mapping (SLAM) strategies. In comparison with video cameras, also used in visual structure from motion algorithms [13], LiDARs offer better depth resolution, range, and horizontal field of view at the cost of lower angular and vertical resolution.

The sensor-based control approach proposed in this paper does not aim at providing a localization algorithm, but rather to devise simple and reliable sensor-based trajectory tracking control methodologies, which can enable the automatic inspection of large infrastructures, under mild geometric assumptions. It is assumed that no reliable GPS signal is available, as near large infrastructures antenna shadowing and multipath problems can severely degrade the signal quality, but both the absolute attitude and the 3-D position of the vehicle relative to an inspection target can be accurately measured resorting to an inertial measurement unit (IMU) and

a 2-D LiDAR sensor (which can provide horizontal profiles of the environment as well as the distance to the ground using a mirror). This sensor-based control approach relies on the formulation of a nonlinear LiDAR-based kinematics for the position of the vehicle relative to the structure. A trajectory-dependent error space is then defined to express the dynamic model of the vehicle, which should be driven to zero by the trajectory tracking controller to be designed, and the flight envelope is partitioned into a set of overlapping regions of operation, for which an LPV representation with piecewise affine dependence (a linear transformation followed by a translation) on the parameters is considered. By imposing an affine parameter dependent structure, a continuous-time state feedback controller can be derived in order to guarantee stability and \mathcal{H}_2 -norm performance bound over a polytopic set of parameters using a finite number of LMIs, and the overall controller is implemented within the framework of gain-scheduling control theory using the D-methodology to switch between controllers [14].

In summary, the main contributions of this paper are: i) the formulation of a LiDAR-based kinematics for aerial vehicles; ii) the formulation of a sensor-based trajectory tracking error space dynamics; iii) the design of trajectory tracking controllers based on gain-scheduling theory, LPV model representation, and LMI controller design tools extended for polytopic systems; and iv) the validation with realistic simulation and experimental results. Relative to the preliminary versions of this work that can be found in [15], [16], and [17], this paper introduces a different vehicle model, redefines the error-space parametrization to better suit the particular characteristic of rotorcraft at low speed trimming trajectories, extends the simulation results, and provides experimental validation for the proposed algorithms. Similar work using a quadrotor for vertical pier inspection has been addressed in [18], [19], where the authors use either LiDAR or a camera to control the horizontal position of the vehicle. Beyond the contributions highlighted above, the strategy presented here (and in the preliminary versions) formulates the control problem on the space of the sensors and uses a gain-switching control methodology that considers different operating regimes over the vehicle's flight envelope, which may lead to better performance and stability guarantees in the same operating conditions.

The paper is organized as follows. The model of a general rotorcraft is presented in Section II, while in Section III the LiDAR kinematics and error space are introduced. The control synthesis and implementation details are provided in Section IV, preceding the simulation and experimental results in Section V. Finally, the concluding remarks and directions of further work are given in Section VI.

II. ROTORCRAFT DYNAMIC MODEL

This section summarizes the rotorcraft dynamic model, in particular, for quadrotors [20], [21]. A comprehensive coverage of rotorcraft flight dynamics can be found in [22], [23] which can be adapted for quadrotor and multirotor vehicles, as done in [24].

The vehicle is modeled as a rigid-body driven by forces and moments applied at its center of mass, which include

the contribution of the rotors, fuselage, and gravity. In order to properly define the rigid-body kinematics and dynamics, consider the definition of an Earth-fixed reference frame $\{E\}$ (neglecting the Earth's rotation rate), using a local tangent plane to the Earth's surface of the reference ellipsoid at a convenient location and using the north-east-down (NED) convention, in which the x -axis of the coordinate frame points north, the y -axis points east, and the z -axis points towards the center of the Earth. To describe the relative motion of the vehicle, a body-fixed frame $\{B\}$ is defined with origin at the vehicle's center of mass, with the x -axis pointing forward, the y -axis pointing right, and the z -axis pointing down. The notation used throughout this paper considers that the subscript and superscript in a rotation matrix indicate the original and transformed frames, respectively, whereas the superscript in a vector indicates the frame in which it is described.

A. Rigid-body Dynamics

Considering $SE(3) := \mathbb{R}^3 \times SO(3)$ as the special Euclidean group in 3-D space, then, the pair $({}^E\mathbf{p}_B, {}^E\mathbf{R}) \in SE(3)$ denotes the configuration of $\{B\}$ relative to $\{E\}$, also denoted by (\mathbf{p}, \mathbf{R}) , for the sake of notation simplicity. The rotation matrix $\mathbf{R} \in SO(3)$ can also be parameterized by the ZYX Euler angles $\boldsymbol{\lambda} = [\phi \ \theta \ \psi]^T$, with $\theta \in (-\frac{\pi}{2}, \frac{\pi}{2})$, $\phi, \psi \in \mathbb{R}$. These parameters can readily be defined by using $\mathbf{R}(\boldsymbol{\lambda}) = \mathbf{R}_z(\psi) \mathbf{R}_y(\theta) \mathbf{R}_x(\phi)$, where, for instance, $\mathbf{R}_x(\cdot)$ denotes the basic rotation of a given angle about the x -axis. In addition, let the linear and angular velocities of $\{B\}$ relative to $\{E\}$, expressed in $\{B\}$, be given by ${}^B\mathbf{v}_B = [u \ v \ w]^T$ and ${}^B\boldsymbol{\omega}_B = [p \ q \ r]^T$, respectively, which are also denoted as \mathbf{v} and $\boldsymbol{\omega}$ for simplicity of notation. Then, the kinematic equations of motion of a generic rigid-body can be written as

$$\begin{cases} \dot{\mathbf{p}} = \mathbf{R}(\boldsymbol{\lambda}) \mathbf{v} \\ \dot{\boldsymbol{\lambda}} = \mathbf{Q}(\boldsymbol{\lambda}) \boldsymbol{\omega} \end{cases} \quad (1a) \quad (1b)$$

where matrix $\mathbf{Q}(\boldsymbol{\lambda}) := \mathbf{Q}(\phi, \theta)$ relates the vehicle angular velocity with the time derivative of the Euler angles. To avoid singularities that may happen when using Euler angles, the attitude kinematics can also be defined in the special orthogonal group, $SO(3)$, as $\dot{\mathbf{R}} = \mathbf{R} \mathbf{S}(\boldsymbol{\omega})$, where the operator $\mathbf{S}(\cdot)$ denotes a skew-symmetric matrix such that $\mathbf{S}(\mathbf{a}) \mathbf{b}$ represents the cross product $\mathbf{a} \times \mathbf{b}$, for some $\mathbf{a}, \mathbf{b} \in \mathbb{R}^3$.

The dynamics of a rigid-body are described by the Newton-Euler equations of motion, which, considering that $\{B\}$ is coincident with the center of mass and explicitly showing the dependence on the Earth's gravity force, can be written as

$$\begin{bmatrix} \mathbf{f}_{ext} + m \mathbf{g} \\ \mathbf{n}_{ext} \end{bmatrix} = \begin{bmatrix} m \mathbf{I}_3 & \mathbf{0} \\ \mathbf{0} & \mathbf{J}_B \end{bmatrix} \begin{bmatrix} \dot{\mathbf{v}} \\ \dot{\boldsymbol{\omega}} \end{bmatrix} + \begin{bmatrix} m \mathbf{S}(\boldsymbol{\omega}) \mathbf{v} \\ \mathbf{S}(\boldsymbol{\omega}) \mathbf{J}_B \boldsymbol{\omega} \end{bmatrix}, \quad (2)$$

where m is the mass of the body, \mathbf{J}_B is the tensor of inertia about frame $\{B\}$, the external forces and moments acting on the rigid-body are respectively denoted by \mathbf{f}_{ext} and \mathbf{n}_{ext} , the gravitational acceleration vector expressed in body coordinates is denoted by $\mathbf{g} = \mathbf{g}(\phi, \theta) := g \mathbf{R}^T \mathbf{e}_3 = g \mathbf{R}_x^T(\phi) \mathbf{R}_y^T(\theta) \mathbf{e}_3$, g stands for the earth gravity acceleration (assumed constant), and $\mathbf{e}_3 = [0 \ 0 \ 1]^T$.

B. Rotorcraft Dynamics

Building on the rigid-body dynamics introduced above, the rotorcraft nonlinear dynamics can be obtained by defining the external forces and moments as functions of the control vector, \mathbf{u} , the linear and angular velocity of the vehicle, and the wind velocity vector, \mathbf{v}_w , described in $\{B\}$. Most rotorcraft vehicles, such as traditional helicopters and most multirotor vehicles, use a thrust force along the vehicle's vertical axis in addition to three independent torques, one for each body rotation axis, as the main way to maneuvering towards a given trajectory. With the emergence of a multitude of commercially available rotorcraft vehicles, such as the Ascending Technologies Pelican or the Mikrocopter QuadroXL quadrotors [25], [26], many control strategies try to benefit from the existence of a well tuned inner-loop system that controls the attitude of the vehicle, tuned for the specific motors and their respective performance characteristics.

Given the typical on-board processing limitations of the proprietary inner-loop, it is customary to implement simple attitude controllers, such as those with proportional-derivative (PD) or proportional-integral-derivative (PID) action, possibly, with feedback linearization terms to simplify and have stability guarantees for the resulting closed-loop dynamics. These controllers usually receive as inputs attitude references in roll/pitch and angular velocity references in yaw, changing the velocities of the rotors to generate the necessary torques.

Considering the angular dynamics in Eq. (2) and the angular kinematics of Eq. (1b), using a stabilizing control law such as

$$\mathbf{n}_{ext} = \mathbf{S}(\boldsymbol{\omega}) \mathbf{J}_B \boldsymbol{\omega} + \mathbf{J}_B \mathbf{Q}^{-1}(\boldsymbol{\lambda}) [\dot{\mathbf{Q}}(\boldsymbol{\lambda}) \boldsymbol{\omega} - \mathbf{K}_2 (\dot{\boldsymbol{\lambda}} - \mathbf{e}_3 \mathbf{e}_3^T \mathbf{u}_{IL}) - \mathbf{\Pi}_{\mathbf{e}_3}^T \mathbf{K}_1 \mathbf{\Pi}_{\mathbf{e}_3} (\boldsymbol{\lambda} - \mathbf{u}_{IL})] \quad (3)$$

the resulting angular inner-loop system is given by

$$\ddot{\boldsymbol{\lambda}} = -\mathbf{K}_2 (\dot{\boldsymbol{\lambda}} - \mathbf{e}_3 \mathbf{e}_3^T \mathbf{u}_{IL}) - \mathbf{\Pi}_{\mathbf{e}_3}^T \mathbf{K}_1 \mathbf{\Pi}_{\mathbf{e}_3} (\boldsymbol{\lambda} - \mathbf{u}_{IL}), \quad (4)$$

where $\mathbf{\Pi}_{\mathbf{e}_3} = [\mathbf{I}_2 \quad \mathbf{0}_{2 \times 1}]$, $\mathbf{K}_1 = \text{diag}(k_\phi, k_\theta)$ and $\mathbf{K}_2 = \text{diag}(k_{\dot{\phi}}, k_{\dot{\theta}}, k_{\dot{\psi}})$ are positive definite matrices, and the inner-loop input vector is denoted as $\mathbf{u}_{IL} = [u_\phi \quad u_\theta \quad u_{\dot{\psi}}]^T$, accounting for the desired roll angle, pitch angle, and yaw angular rate, respectively. The resulting system is linear and the state variables ϕ , θ , and $\dot{\psi}$ converge exponentially to constant input references u_ϕ , u_θ , and $u_{\dot{\psi}}$, respectively. This result can be derived using a feedback linearization strategy, as detailed in [27].

Finally, considering that $\boldsymbol{\omega}$ is related with $\dot{\boldsymbol{\lambda}}$ according to (1b), the velocity dynamics equation can be written as

$$\dot{\mathbf{v}} = -\mathbf{S}(\boldsymbol{\omega}) \mathbf{v} + \mathbf{g}(\phi, \theta) - m^{-1} (u_T \mathbf{e}_3 + \mathbf{f}_D(\mathbf{v}, \mathbf{v}_w)) \quad (5)$$

where \mathbf{v}_w denotes the wind velocity disturbance and $\mathbf{f}_D(\mathbf{v}, \mathbf{v}_w)$ accounts for the drag effects acting on the vehicle, which can either be computed using computational fluid dynamics software or wind tunnel testing.

C. Equilibrium Trajectories

The dynamic equilibrium of a rigid-body requires that the net sum of the external forces and moments acting on the body are zero. This implies that the linear and angular velocities

expressed in the body frame can assume non-zero but constant values while the accelerations are required to be zero. A trimming or equilibrium trajectory of a vehicle, denotes the kinematic component of the state for which the dynamic component of the state remains in the equilibrium set. For the considered class of vehicles and for each trimming trajectory, the variables $\mathbf{v}_C, \dot{\boldsymbol{\lambda}}_C \in \mathbb{R}^3$, $\mathbf{u}_C \in \mathbb{R}^4$, $\phi_C, \theta_C \in \mathbb{R}$, respectively denote the constant trimming values of the linear velocity, Euler angles vector derivative, input vector, roll angle, and pitch angle. The trimming trajectory components are denoted by $\mathbf{p}_C(\cdot) : \mathbb{R}_+ \rightarrow \mathbb{R}^3$ and $\boldsymbol{\lambda}_C(\cdot) = [\phi_C, \theta_C, \psi_C(\cdot)]^T$, with $\psi_C(\cdot) : \mathbb{R}_+ \rightarrow \mathbb{R}$, implying that the yaw angle, $\psi_C(\cdot)$, can change without violating the equilibrium condition, although satisfying a constant rate imposed by $\dot{\psi}_C = u_{\dot{\psi}}$. As shown in [28], the set of achievable trimming trajectories, \mathcal{E} , corresponds to straight lines and z -aligned helices described by the vehicle with arbitrary, but constant, linear velocity and yaw angle relative to the path.

Further consider an additional frame, denoted as the horizontal body-fixed frame, $\{H\}$, such that ${}^E \mathbf{p}_H = \mathbf{p}$ denotes the position of frame $\{H\}$ described in frame $\{E\}$, ${}^E \mathbf{R}_H := \mathbf{R}_z(\psi)$ is the rotation from frame $\{H\}$ to frame $\{E\}$, and ${}^H \mathbf{R}_B := \mathbf{R}_y(\theta) \mathbf{R}_x(\phi)$ the rotation from frame $\{B\}$ to frame $\{H\}$. A versatile parametrization can be introduced by using the velocity vector described in the horizontal body-fixed frame $\{H\}$, ${}^H \mathbf{v}_C = \mathbf{R}_y(\theta_C) \mathbf{R}_x(\phi_C) \mathbf{v}_C$, combined with the yaw angular velocity, $\dot{\psi}_C$, yielding

$$\boldsymbol{\xi} = [{}^H \mathbf{v}_C^T \quad \dot{\psi}_C]^T = [{}^H u_C \quad {}^H v_C \quad {}^H w_C \quad \dot{\psi}_C]^T. \quad (6)$$

III. SENSOR-BASED ERROR DYNAMICS

The use of sensor-based controllers is most useful when the relative position measurements are more accurate than the available absolute position measurements. This is the case of the close inspection of an infrastructure, where the visibility of the GPS satellite constellation is compromised, whereas the accuracy of LiDAR sensors increases with the proximity to the infrastructure. Thus, it is assumed that there is no access to absolute position measurements, but accurate estimates of the body velocities and attitude are available, which might be obtained using optical flow sensors and IMUs. Without loss of generality, the LiDAR is assumed to be at the center and aligned with the body-fixed frame, as the transformation between the LiDAR frame and $\{B\}$ is known.

A. Pier Geometry and Center Position

Consider that at each sampling instant, the horizontally mounted LiDAR provides a set of n_L data points in frame $\{B\}$, from which a subset is selected as the region of interest for control purposes, $(\rho_{B_i}, \alpha_{B_i})$, for $i = 1, \dots, n$, where ρ_{B_i} stands for the range distance measurement and α_{B_i} is the respective bearing. It is assumed that the inspection targets are approximately cylindrical, which includes many bridge piers, industrial chimneys, wind turbine towers, etc. Although the methodology proposed hereafter considers piers with circular section, it can also tackle piers with sections described by an ellipse or a rectangle, at the cost of a degradation of trajectory tracking performance, as will be discussed later.

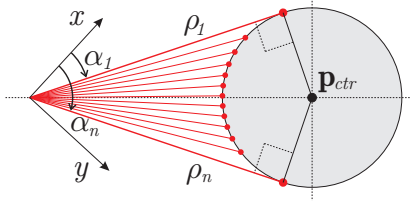


Fig. 2. Laser measurements intersecting the pier.

The main goal is to detect invariant points, or landmarks, from which we can infer the relative position of the vehicle. As this task is more challenging in frame $\{B\}$, the original measurements of the LiDAR in frame $\{B\}$ are transformed and projected into frame $\{H\}$, where they are denoted as (ρ_i, α_i) . The relation between range and angular information in $\{B\}$ and their projection into $\{H\}$ can be expressed as

$$\begin{aligned} \rho_i^2 &= \rho_{B_i}^2 [(\cos \alpha_{B_i} \cos \theta + \sin \alpha_{B_i} \sin \phi \sin \theta)^2 + (\sin \alpha_{B_i} \cos \phi)^2] \\ \alpha_i &= \text{atan2}(\sin \alpha_{B_i} \cos \phi, \cos \alpha_{B_i} \cos \theta + \sin \alpha_{B_i} \sin \phi \sin \theta) \end{aligned}$$

where $\text{atan2}(\cdot, \cdot)$ denotes the four quadrant inverse of the tangent function. It is straightforward to see that the intersection of any vertical cylindrical pier with the xy -plane of frame $\{H\}$ yields a circle. In this way, the laser measurements (ρ_i, α_i) that represent the pier also represent an arc of a circle. Using basic notions of geometry, it can be seen that, given any point outside the circle and in the same plane, there are only two lines that pass through this point and are tangent to the circle, as shown in Fig. 2. These lines are approximated by the first and last laser measurements that intersect the pier, provided that the angular resolution of the laser is sufficiently high, which is typically below 0.25 degrees. Therefore, the center of the pier can be estimated using the first and last laser measurements transformed into the $\{H\}$ frame, respectively (ρ_1, α_1) and (ρ_n, α_n) , where n is the number of laser measurements that intersect the pier. The expressions for the equivalent range and angle of the center of the pier, respectively denoted as ρ and α , are given by

$$\rho = \frac{\rho_1 + \rho_n}{2 \cos(\frac{\alpha_n - \alpha_1}{2})}, \quad \alpha = \frac{\alpha_1 + \alpha_n}{2}. \quad (7)$$

The fact that only the first and last measurements of the laser are used to estimate the center of the pier indicates that if its shape is not exactly a cylinder, the algorithm will still be valid. The deviations from the desired trajectory can be regarded as a consequence of a perturbation to the nominal system, as the center of the pier measured by the laser will not correspond exactly to the real value.

In order to have a complete 3-D position measurement, an additional altitude sensor is necessary. In the approach presented in this paper, part of the horizontal LiDAR profile is deflected towards the ground using a mirror, thus providing a good measurement of distance to the ground along the z -axis of the sensor frame $\{B\}$, without additional sensors. Further assuming that the ground surrounding the inspection area is planar and horizontal, together with the fact that the pitch and roll angles are available, the distance-to-ground measurement

in frame $\{B\}$, denoted as z_{B_g} , can be easily projected into the z -axis of frame $\{H\}$ using $z_g = z_{B_g} \cos \phi \cos \theta$.

Note that the horizontal ground assumption, which is somewhat restrictive, could be easily overcome with the use of an additional laser scanner placed in the yz -plane of frame $\{B\}$, replacing the range only sensor in the z -axis.

B. LiDAR Kinematics

The equations of motion for the LiDAR kinematics are naturally divided into the horizontal plane and the vertical axis kinematics. Nonetheless, they can be considered as a unique sensor that provides the position of the center of the pier at ground level, \mathbf{p}_p , which can be expressed as $\mathbf{p}_p = \mathbf{R}_z(\alpha) [\rho \ 0 \ z_g]^T$, or as $\mathbf{p}_p = {}^H \mathbf{R}({}^E \mathbf{p}_p - {}^E \mathbf{p}_B)$. Defining the generalized LiDAR-based position vector as $\boldsymbol{\eta} = [\rho \ \alpha \ z_g]^T$, after some algebraic manipulation, the LiDAR-based kinematics equation can be written as

$$\dot{\boldsymbol{\eta}} = \mathbf{r}_\eta(r) - \mathbf{I}_\eta(\rho) \mathbf{R}_z^T(\alpha) \mathbf{R}_y(\theta) \mathbf{R}_x(\phi) \mathbf{v}, \quad (8)$$

where $\mathbf{r}_\eta(r) = [0 \ -r \ 0]^T$, ${}^H \mathbf{R} = \mathbf{R}_y(\theta) \mathbf{R}_x(\phi)$, and $\mathbf{I}_\eta(a) = \text{diag}([1 \ 1/a \ 1])$, for all $a \neq 0$. Thus, this new position kinematics equation can be used to replace (1a) and formulate a trajectory dependent error space to be used in a sensor-based control synthesis.

C. Error Dynamics

Consider the vehicle equations of motion presented in (1b), (4), and (5), as well as the sensor-based position kinematics (8), denoting the desired trimming values for the state and input vectors as \mathbf{v}_c , $\boldsymbol{\eta}_c(\cdot)$, $\dot{\boldsymbol{\lambda}}_c$, $\boldsymbol{\lambda}_c(\cdot)$, and \mathbf{u}_c . For the envisioned applications, the trimming trajectories of interest are z -aligned helices and hover, which are characterized by constant values of range and bearing of the pier center in frame $\{H\}$, denoted as ρ_c and α_c . This subset of the possible trimming trajectories, $\mathcal{E}_L \subset \mathcal{E}$, can be described by the parameterization $\boldsymbol{\xi}_L = [\rho_c \ \alpha_c \ {}^H w_c \ \dot{\psi}_c]^T$, where ${}^H w_c$ is the desired z -component of the velocity vector described in $\{H\}$. This parameterization can be mapped onto the more general parameterization already introduced in (6), considering that ${}^H \mathbf{v}_c = \mathbf{R}_z(\alpha_c) [0 \ -\rho_c \dot{\psi}_c \ {}^H w_c]^T$.

Defining the LiDAR-based state vector as $\mathbf{x}_L = [\mathbf{v}^T, \boldsymbol{\eta}^T, \dot{\boldsymbol{\lambda}}^T, \boldsymbol{\lambda}^T]^T \in \mathbb{R}^{12}$, the error vector can be simply defined as $\mathbf{x}_e = \mathbf{x}_L - \mathbf{x}_c$, where \mathbf{x}_c is the desired state trajectory. Let also $\mathbf{u}_e = \mathbf{u} - \mathbf{u}_c$ and $\mathbf{v}_{w_e} = \mathbf{v}_w$, which considers that there is no disturbance at trimming, $\mathbf{v}_{w_e} = 0$. Then, in the new error coordinate system, it can be shown that the linearization of the sensor-based dynamics given by (1b), (4), (5), and (8) along a trimming trajectory is time invariant, following the approach in [8] and [28], and noting that $\dot{\boldsymbol{\eta}}_c = [0 \ 0 \ {}^H w_c]^T$ and $\dot{\boldsymbol{\lambda}}_c = [0 \ 0 \ \dot{\psi}_c]^T$, the nonlinear error dynamics can then be expressed as

$$\dot{\mathbf{x}}_e = \mathbf{f}_e(\mathbf{x}_e, \mathbf{u}_e, \mathbf{v}_w, \mathbf{x}_c, \mathbf{u}_c) = \begin{bmatrix} \dot{\mathbf{v}} \\ \dot{\boldsymbol{\eta}} - \dot{\boldsymbol{\eta}}_c \\ \dot{\boldsymbol{\lambda}} \\ \dot{\boldsymbol{\lambda}} - \dot{\boldsymbol{\lambda}}_c \end{bmatrix}. \quad (9)$$

The linearization of (9) about the origin, or equivalently, the linearization of (1b), (4), (5), and (8) about the trimming trajectory can be expressed in the generalized error space as

$$\delta \dot{\mathbf{x}}_e = \mathbf{A}_e^\xi \delta \mathbf{x}_e + \mathbf{B}_e^\xi \delta \mathbf{u}_e + \mathbf{B}_{w_e}^\xi \delta \mathbf{w}_e \quad (10)$$

where $\mathbf{A}_e^\xi = \frac{\partial}{\partial \mathbf{x}} \mathbf{f}_e(\cdot) \Big|_{\boldsymbol{\xi}}$ is a constant matrix for each trimming trajectory defined by $\boldsymbol{\xi}$, considering similar definitions for \mathbf{B}_e^ξ and $\mathbf{B}_{w_e}^\xi$. For a small enough region of operation, the nonlinear system can be accurately approximated by a linear parameter varying (LPV) system, that continuously depend on the parameter vector $\boldsymbol{\xi}$. Introducing the output vector to be controlled \mathbf{z} , the general exogenous input vector \mathbf{w} , and redefining the state and input vectors as $\mathbf{x} = \delta \mathbf{x}_e$ and $\mathbf{u} = \delta \mathbf{u}_e$, an LPV system can be defined as

$$\begin{cases} \dot{\mathbf{x}} = \mathbf{A}(\boldsymbol{\xi})\mathbf{x} + \mathbf{B}_w(\boldsymbol{\xi})\mathbf{w} + \mathbf{B}\mathbf{u} \\ \mathbf{z} = \mathbf{C}\mathbf{x} + \mathbf{D}\mathbf{w} + \mathbf{E}\mathbf{u} \end{cases} \quad (11a)$$

$$(11b)$$

Thus, it follows that there is a linear time invariant plant (11), associated with each trimming trajectory $\boldsymbol{\xi} \in \mathcal{E}_L$, for which a linear controller can be designed.

Recalling the terms of the dynamic equations (4) and (5) that depend on the input vector \mathbf{u} , it can be seen that the resulting linearized error space matrix \mathbf{B} is constant for every trimming trajectory, resulting in an exact representation.

IV. CONTROLLER DESIGN

In this section a LMI approach is used to tackle the continuous-time state feedback \mathcal{H}_2 synthesis problem for polytopic LPV systems such as (11). The system is parameterized by $\boldsymbol{\xi}$, which is a possibly time-varying parameter vector and belongs to the convex set $\mathcal{E}^j = \text{co}(\mathcal{E}_0^j)$. Here, the operator $\text{co}(\cdot)$ denotes the convex hull of the elements of the argument set, $\mathcal{E}_0^j = \{\boldsymbol{\xi}_1, \dots, \boldsymbol{\xi}_{n_j}\}$, where $\boldsymbol{\xi}_1$ to $\boldsymbol{\xi}_{n_j}$ are the vertices of a polytope. It is also noted that the controller synthesis presented in the following subsection will only be valid for a specific operating region, here represented by $\mathcal{E}^j \subset \mathcal{E}$.

A. Synthesis

Applying the static state feedback law given by $\mathbf{u} = \mathbf{K}\mathbf{x}$ to (11) results in the closed-loop $\mathbf{T}_{zw}(\boldsymbol{\xi})$. It can be seen that testing for stability or solving the synthesis problem without any further result, involves an infinite number of LMIs. Thus, several different structures for LPV systems have been proposed which reduce the problem to that of solving a finite number of LMIs. An affine polytopic description is adopted, which can also be used to model a wide spectrum of systems and, as shown in the results presented in Section V, is an adequate choice for the system at hand.

Definition 1 (Affine polytopic LPV). *The system (11) is said to be a polytopic LPV system if the system matrix verifies $\mathbf{P}(\boldsymbol{\xi}) \in \text{co}(\mathbf{P}_1, \dots, \mathbf{P}_{n_r})$ for all $\boldsymbol{\xi} \in \mathcal{E}^j$, $i = 1, \dots, n_j$, where*

$$\mathbf{P}(\boldsymbol{\xi}) = \begin{bmatrix} \mathbf{A}(\boldsymbol{\xi}) & \mathbf{B}_w(\boldsymbol{\xi}) & \mathbf{B}(\boldsymbol{\xi}) \\ \mathbf{C}(\boldsymbol{\xi}) & \mathbf{D}(\boldsymbol{\xi}) & \mathbf{E}(\boldsymbol{\xi}) \end{bmatrix}, \quad \mathbf{P}_i = \begin{bmatrix} \mathbf{A}_i & \mathbf{B}_{w_i} & \mathbf{B}_i \\ \mathbf{C}_i & \mathbf{D}_i & \mathbf{E}_i \end{bmatrix}.$$

Moreover, if \mathcal{E}^j is a polytopic set, such as $\mathcal{E}^j = \text{co}(\mathcal{E}_0^j)$, $\mathcal{E}_0^j = \{\boldsymbol{\xi}_1, \dots, \boldsymbol{\xi}_{n_j}\}$, and $\mathbf{P}(\boldsymbol{\xi})$ depends affinely on $\boldsymbol{\xi}$, then $\mathbf{P}_i =$

$\mathbf{P}(\boldsymbol{\xi}_i)$ for all $i = 1, \dots, n_j$, i.e., the vertices of the parameter set can be uniquely identified with the vertices of the system.

Using this polytopic structure with [6, Proposition 1.19], the quadratic stability of the system for a given region of operation can be established if a certain Lyapunov equation of the closed-loop system can be satisfied for all for all $\boldsymbol{\xi} \in \mathcal{E}_0^j$.

The \mathcal{H}_2 synthesis problem can be described as that of finding a control matrix \mathbf{K} that stabilizes the closed-loop system and minimizes the \mathcal{H}_2 -norm of $\mathbf{T}_{zw}(\boldsymbol{\xi})$, denoted by $\|\mathbf{T}_{zw}(\boldsymbol{\xi})\|_{\mathcal{H}_2}$. It is assumed that matrix $\mathbf{D}(\boldsymbol{\xi}) = 0$ in order to guarantee that $\|\mathbf{T}_{zw}(\boldsymbol{\xi})\|_{\mathcal{H}_2}$ is finite for every internally stabilizing and strictly proper controller. The following theorem is used for controller design and relies on results available in [5] and [6], after being rewritten for the case of polytopic LPV systems. In the following, $\text{tr}(\cdot)$ denotes the trace of the argument matrix.

Theorem 1 (Polytopic stability). *If there are real matrices $\mathbf{X} = \mathbf{X}^T \succ 0$, $\mathbf{Y} \succ 0$, and \mathbf{W} such that*

$$\begin{bmatrix} \mathbf{A}(\boldsymbol{\xi})\mathbf{X} + \mathbf{X}\mathbf{A}^T(\boldsymbol{\xi}) + \mathbf{B}(\boldsymbol{\xi})\mathbf{W} + \mathbf{W}^T\mathbf{B}^T(\boldsymbol{\xi}) & \mathbf{B}_w(\boldsymbol{\xi}) \\ & \mathbf{B}_w^T(\boldsymbol{\xi}) \\ & & -\mathbf{I} \end{bmatrix} \prec 0 \quad (12a)$$

$$\begin{bmatrix} \mathbf{Y} & \mathbf{C}(\boldsymbol{\xi})\mathbf{X} + \mathbf{E}(\boldsymbol{\xi})\mathbf{W} \\ \mathbf{X}\mathbf{C}^T(\boldsymbol{\xi}) + \mathbf{W}^T\mathbf{E}^T(\boldsymbol{\xi}) & \mathbf{X} \end{bmatrix} \succ 0 \quad (12b)$$

$$\text{tr}(\mathbf{Y}) < \gamma^2 \quad (12c)$$

for all $\boldsymbol{\xi} \in \mathcal{E}_0^j$, where $\mathbf{K} = \mathbf{W}\mathbf{X}^{-1}$, then, the closed-loop system is quadratically stable and there exists an upper-bound γ for the continuous-time \mathcal{H}_2 -norm of the closed-loop operator, i.e., $\|\mathbf{T}_{zw}(\boldsymbol{\xi})\|_{\mathcal{H}_2} < \gamma$ for all $\boldsymbol{\xi} \in \mathcal{E}^j$.

Proof. As a proof outline, it can be seen that satisfying the LMI system for all $\boldsymbol{\xi} \in \mathcal{E}_0^j$ is equivalent to satisfying the same system of LMIs for all $\boldsymbol{\xi} \in \mathcal{E}^j$, as the system (11) is a polytopic LPV system. The proof that satisfying (12) implies $\|\mathbf{T}_{zw}(\boldsymbol{\xi})\|_{\mathcal{H}_2} < \gamma$ for all $\boldsymbol{\xi} \in \mathcal{E}^j$ can be obtained from the definition of \mathcal{H}_2 -norm of $\mathbf{T}_{zw}(\boldsymbol{\xi})$. Further details and the complete proof of this result are provided in [27]. \square

With this result, the optimal solution for the continuous-time \mathcal{H}_2 control problem is approximated through the minimization of γ subject to the LMIs of Theorem 1.

B. Implementation

To guarantee that the closed-loop system has zero steady-state error in position and yaw angle, the integral of the output vector $\mathbf{y}_e = [\boldsymbol{\eta}_e^T \quad \psi_e]^T$ is included in the design as a performance output, augmenting the state dynamics with the equation $\dot{\mathbf{x}}_i = \mathbf{y}_e$. To meet the design requirements, the weighting function associated with the integral state is chosen as $\mathbf{W}_1 = \text{diag}(5, 5, 3, 7)$, the actuation weight is $\mathbf{W}_2 = \text{diag}(15\mathbf{I}_3, 3)$, and the state weight is given by $\mathbf{W}_3 = \text{diag}(0.01\mathbf{I}_6, 5\mathbf{I}_3, 0.01\mathbf{I}_2, 5)$. Additionally, dynamic weights are used for the actuation vector \mathbf{u} , so that higher actuation frequencies are penalized, as well as for the disturbance process \mathbf{w} to represent the Von Karman disturbance model transfer functions (see [22] and references therein).

The parameter vector for the sensor-based control approach, previously defined as $\boldsymbol{\xi}_L = [\rho_C \ \alpha_C \ {}^H w_C \ \dot{\psi}_C]$, is considered to parameterize a subset, \mathcal{E}_L , of all possible trimming trajectories, \mathcal{E} . For the implementation of the overall controller within the framework of the gain scheduling theory, the set of trimming trajectories \mathcal{E}_L is partitioned into $n_r = 128$ overlapping polytopic regions of operation, \mathcal{E}^j for $j = 1, \dots, n_r$, such that the union of all operating regions completely covers the set of trimming trajectories. The controller implementation is based on the D-methodology, comprehensively described in [14], which moves all integrators to the plant input, and adds differentiators where needed to preserve the transfer functions and the stability characteristics of the closed-loop system. The bump-less transfer property of this implementation methodology allows for the controller to switch between regions of operation without having to interpolate between controllers.

The gain-switching controller is therefore defined by partitioning $\rho_C \in [0.4, 2]$ m into 2 intervals; $\alpha_C \in [-135, 135]$ deg into 8 intervals; $\dot{\psi}_C \in [-40, 40]$ deg/s into 4 intervals; and ${}^H w_C \in [-0.5, 0.5]$ m/s into 2 intervals. The operating regions spanned by the interval $\alpha_C \in [-135, 135]$ deg is coincident with the field-of-view of the Hokuyo LiDAR used in the experimental results, thus, if another sensor with increased field-of-view is used, the flight envelope can be easily extended.

The state-space nonlinear system is approximated by affine functions on the parameters $\boldsymbol{\xi} \in \mathcal{E}^j$, for $j = 1, \dots, n_r$, using least squares fitting. The error introduced by this approximation can be evaluated by comparing, for each $\boldsymbol{\xi}$, the resulting LPV system matrices, e.g., $\mathbf{A}(\boldsymbol{\xi})$, with the linearization of the nonlinear system at the same point, $\mathbf{A}_{NL}(\boldsymbol{\xi}) := \left. \frac{\partial \mathbf{f}}{\partial \mathbf{x}} \right|_{\boldsymbol{\xi}}$. Noting that similar definitions can be used for each system matrix, this error can be defined as

$$\tilde{A}(\boldsymbol{\xi}) = 100 \frac{\|\mathbf{A}_{NL}(\boldsymbol{\xi}) - \mathbf{A}(\boldsymbol{\xi})\|_F}{\|\mathbf{A}_{NL}(\boldsymbol{\xi})\|_F},$$

considering that $\|\cdot\|_F$ is the Frobenius norm of the argument matrices. In practice, a finite number of points in a given zone j is used for the respective LPV approximation, which can be defined as $\hat{\mathcal{E}}^j := \{\boldsymbol{\xi}_1, \dots, \boldsymbol{\xi}_{n^j}\}$, and amounts to $n^j = 7^4 = 2401$ points for each of the n_r regions of operation used in the presented results. Thus, the maximum approximation error for a given region \mathcal{E}^j can be defined as $\tilde{A}_{max}^j = \max_{\boldsymbol{\xi}_i \in \hat{\mathcal{E}}^j} \tilde{A}(\boldsymbol{\xi}_i)$. These indicators for the presented case show that the average maximum errors throughout the n_r regions is 0.3% in the case of matrix \mathbf{A} , and 9.4% for matrix \mathbf{B}_w , while the maximum errors are respectively 0.53% and 12.5%, noting that \mathbf{B} has no approximation error, as mentioned in Section III-C.

V. SIMULATION AND EXPERIMENTAL RESULTS

To further validate the proposed strategy, experimental trials were conducted at the Sensor-based Cooperative Robotics Research (SCORE) laboratory, University of Macau. The setup consists of an Ascending Technologies Pelican quadrotor with custom processing and interface programs, instrumented with an Hokuyo UTM-30LX 2-D LiDAR to acquire horizontal profiles of the environment, a mock-up scenario of a pier to be inspected, and a VICON motion capture system with 12 cameras [29] (as shown in Figs. 1 and 3), which provides



Fig. 3. LiDAR-based trajectory tracking control: Astec Pelican quadrotor with Hokuyo LiDAR, mock-up pier, and laboratory setup.

accurate estimates of the position, attitude, linear and angular velocities of any vehicle placed inside the working area with the correct markers. Although this quadrotor is fully capable of running the proposed control methodologies within the on-board CPU, a rapid prototyping and testing architecture was used, which runs in the Matlab[®]/Simulink[®] environment and seamlessly integrate the controller and the vehicle through a WiFi UDP communication link. The LiDAR data is acquired on board the vehicle and processed to obtain the sensor-based measurements α and ρ , as well as the altitude of the vehicle using a mirror that deflects the first 50 laser angular positions towards the ground (see Fig. 3). The Pelican internal IMU estimates are used in the proposed controller to obtain the attitude and angular velocity, whereas the vehicle linear velocity is obtained using the VICON system. In the future, this last variable will be obtained using an optical flow sensor, such as the PX4FLOW board [30].

To perform accurate infrastructure inspection, an autonomous quadrotor is required to cover the infrastructure comprehensively in order to detect cracks, corrosion, leaks, or any other indicator that further maintenance procedures are required. Therefore, the required flight envelope is characterized by low speed, high yaw maneuverability, good vertical flight capabilities, and the possibility of describing helices around the infrastructure. To complement the experimental results, this section also provides realistic simulation results in the same conditions as the experimental trials. Two simulation trials were carried out using the nonlinear dynamic quadrotor model presented above: (i) with wind disturbance, and (ii) with no disturbance or measurement noise. In addition to the wind disturbance noise generated using the Von Karman disturbance model, as described in Section IV-B, the simulation scenario presented below also includes a discrete wind gust with amplitude 2.5 m/s in each axis, rising time of 2.5 s, constant direction in the earth-fixed frame, and applied at $t = 36$ s.

Considering the envisioned applications, in the results provided in this paper the vehicle is required to track a trajectory

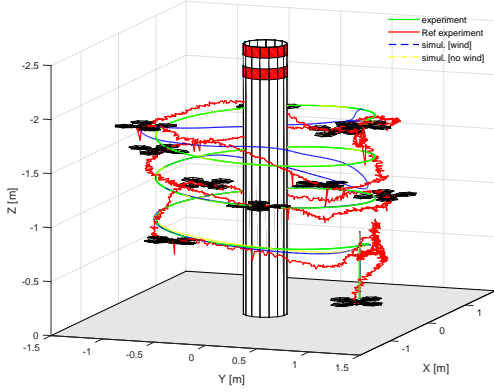
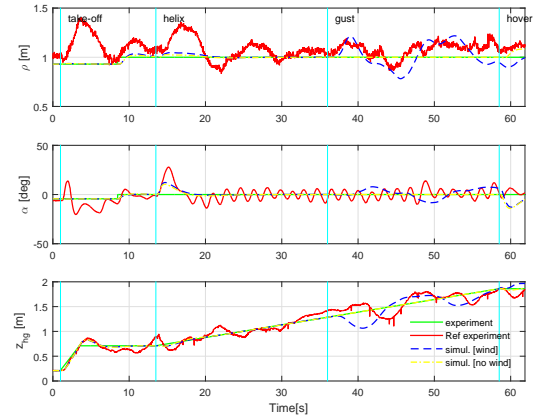


Fig. 4. LiDAR-based trajectory tracking control: scenario and vehicle trajectories, both experimental and simulated (with and without wind disturbance).

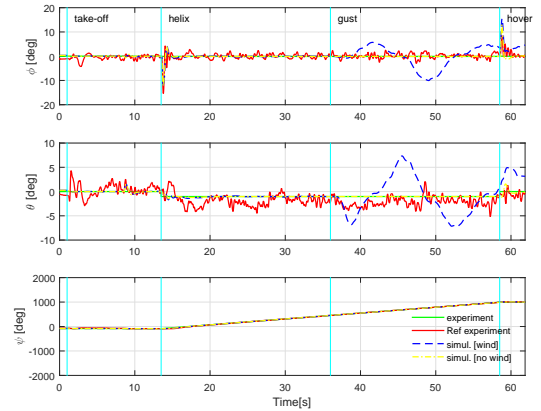
composed of: (i) take off followed by stationary hover at the initial position relative to the pier, with slight transition to the desired initial position, with $\rho_C = 1.0$ m, and $\alpha_C = \dot{\psi}_C = {}^H w_C = 0$; (ii) an ascending helix completing three loops around the pier and keeping the vehicle facing the pier, with $\rho_C = 1.0$ m, $\alpha_C = 0$ deg, $\dot{\psi}_C = 24$ deg/s, and ${}^H w_C = -2.65$ cm/s; (iii) a stationary hover at the final position: $\rho_C = 1.0$ m, and $\alpha_C = \dot{\psi}_C = {}^H w_C = 0$. The sensor-based trajectory tracking results are presented in Figs. 4-7, featuring the laser-based position and attitude, the control action, and the transitions between regions of operation. The instants when the vehicle takes off from the ground, transitions from the initial hover to the ascending helix trajectory, when the wind gust is applied (for the simulation results only), as well as when the vehicle transitions from the ascending helix to a stationary hover at the final position are also represented in these figures with vertical lines, respectively, at $t = 0.0$ s, $t = 13.5$ s, $t = 36$ s, and $t = 58.5$ s. A video that shows the vehicle performing an helix trajectory around the Pier is available at <https://youtu.be/phjW7tHwNCQ>.

It can be seen that the vehicle can adequately handle the transitions from hover to the ascending helix and vice-versa, converging to the desired trajectory as well as attenuating the effects of the wind disturbance and measurement noise, when they exist. This can be observed in Fig. 5, noting that the tracking errors of the simulation results with (without) wind disturbance are lower than 22 cm (8 cm) in ρ , 14 deg (14 deg) in α , and 34 cm (13 cm) in z_g . Regarding the experimental results, it can be seen that the tracking errors are lower than 36 cm in ρ , 28 deg in α , and 24 cm in z_g , not considering the initial take-off. This degradation of performance relative to the simulation results might be attributed to unmodeled dynamics, model parameters not well identified/tuned, high and nonlinear measurement noise, delays introduced by the additional sensor processing, as well as to the controller implementation environment and the communications between the vehicle and Simulink.

After the wind gust is applied in the simulation trials, the actuation has to adapt to the constant direction of the wind gust (in frame $\{E\}$) while changing the vehicle direction to track



(a) Laser-based position η



(b) Euler angles λ

Fig. 5. LiDAR-based trajectory tracking control: position and attitude.

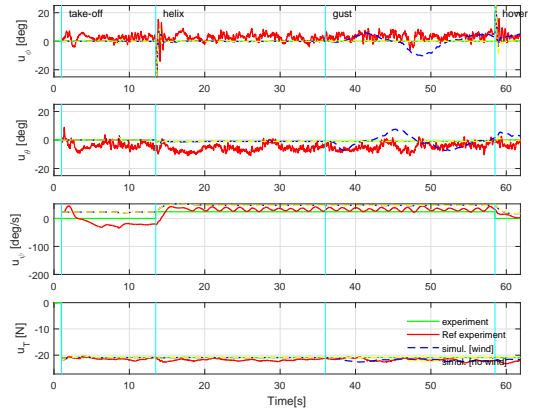


Fig. 6. LiDAR-based trajectory tracking control: control signals.

the reference trajectory, as can be seen in Fig. 6. Nonetheless, the tracking errors remain within the same order of magnitude as those of the transitions from and to hover, even under the influence of the wind gust. Regarding the experimental results, another source of disturbance that is not considered in the model (in particular the wind dynamic weights) is the type of wind disturbance that results from flying the vehicle in a confined space such as the one where the experiments took place. As it is largely studied and acknowledged that the proximity of this type of vehicles with the ground generates

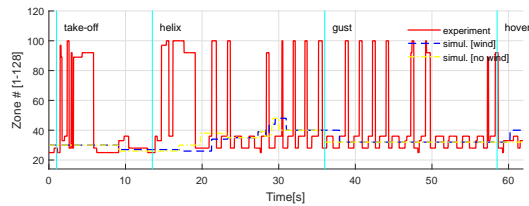


Fig. 7. LiDAR-based trajectory tracking control: active zone.

an increased lift force, similar distances to walls and ceiling will also induce distortions in the air flow generating a wind disturbance that might not be well represented by the Von Karman models. Nevertheless, the controller is able to follow the desired trajectory with acceptable performance while dealing with all these perturbations, as can be seen in the actuation signals of Fig. 6, which are clearly not at trim.

Regarding the operating region transitions, presented in Fig. 7, it can be seen that the higher number of transitions is concentrated on the take-off part of the trajectory, where the vehicle must quickly reach and maintain a stationary hover. Also, the transitions between operating regions (and their respective controller gains) can also be observed during other changes of desired trajectory, consistently showing that the overall gain-switching controller is effective in stabilizing the vehicle and converging to the desired trajectory, even under demanding perturbations.

VI. CONCLUDING REMARKS

This paper presented the design and experimental validation of a LiDAR-based trajectory tracking control methodology for autonomous rotorcraft, considering that no absolute position solution, such as GPS, is available for control. The major contributions of this work are the introduction of a LiDAR-based nonlinear kinematics, formulated in 3-D space, and the definition of a trajectory-dependent error space to express the dynamic model of the vehicle and the sensor-based kinematics. The effectiveness of the proposed control method was validated with experimental results and the performance assessment complemented with simulations, using a nonlinear model of the vehicle and realistic mission scenarios. The quality of the obtained results clearly indicates that the proposed methodologies are well suited to be employed in the automatic inspection of large infrastructures using autonomous rotorcraft. Future work includes the performance evaluation of the proposed controllers during automatic inspection operation near real world infrastructures.

REFERENCES

- [1] G. Parke and N. Hewson, Eds., *ICE Manual of Bridge Engineering*, 2nd ed. London, UK: Institution of Civil Engineers, 2008.
- [2] L. Marconi and R. Naldi, "Robust full degree-of-freedom tracking control of a helicopter," *Automatica*, vol. 43, no. 11, pp. 1909–1920, 2007. [Online]. Available: <http://www.sciencedirect.com/science/article/pii/S0005109807002154>
- [3] B. J. Guerreiro, C. Silvestre, and R. Cunha, "Terrain avoidance nonlinear model predictive control for autonomous rotorcraft," *Journal of Intelligent & Robotic Systems*, vol. 68, no. 1, pp. 69–85, 2012.
- [4] W. J. Rugh and J. S. Shamma, "Research on gain scheduling," *Automatica*, vol. 36, no. 10, pp. 1401–1425, October 2000, survey Paper.
- [5] L. Ghaoui and S.-I. Niculescu, *Advances in Linear Matrix Inequality Methods in Control*. Philadelphia, PA: Society for Industrial and Applied Mathematics, SIAM, 1999.
- [6] C. Scherer and S. Weiland, "Lecture notes on linear matrix inequality methods in control," Dutch Institute of Systems and Control, 2000.
- [7] R. Cunha, D. Antunes, P. Gomes, and C. Silvestre, "A path-following preview controller for autonomous air vehicles," in *AIAA Guidance, Navigation and Control Conference*. Keystone, CO: AIAA, August 2006.
- [8] C. Silvestre, A. Pascoal, and I. Kammer, "On the design of gain-scheduled trajectory tracking controllers," *International Journal of Robust and Nonlinear Control*, vol. 12, no. 9, pp. 797–839, July 2002.
- [9] P. Rosa, "Multiple-model adaptive control of uncertain ltv systems," Ph.D. dissertation, Instituto Superior Técnico, 2011.
- [10] S. Thrun, D. Fox, W. Burgard, and F. Dellaert, "Robust Monte Carlo localization for mobile robots," *Artificial Intelligence*, vol. 128, no. 1-2, pp. 99–141, 2001.
- [11] R. He, S. Prentice, and N. Roy, "Planning in information space for a quadrotor helicopter in a GPS-denied environment," in *IEEE International Conference on Robotics and Automation*, Pasadena, CA, USA, May 2008, pp. 1814–1820.
- [12] B. J. Guerreiro, P. Batista, C. Silvestre, and P. Oliveira, "Globally asymptotically stable sensor-based simultaneous localization and mapping," *IEEE Transactions on Robotics*, vol. 29, no. 6, 2013.
- [13] C. Wu, "Towards linear-time incremental structure from motion," in *International Conference on 3D Vision-3DV, IEEE*, 2013, pp. 127–134.
- [14] I. Kammer, A. Pascoal, P. P. Khargonekar, and E. E. Coleman, "A velocity algorithm for the implementation of gain-scheduled controllers," *Automatica*, vol. 31, no. 8, pp. 1185–1191, 1995.
- [15] B. J. Guerreiro, C. Silvestre, R. Cunha, and D. Antunes, "Trajectory tracking H2 controller for autonomous helicopters: an application to industrial chimney inspection," in *17th IFAC Symposium on Automatic Control in Aerospace*, June 2007.
- [16] B. J. Guerreiro, C. Silvestre, and R. Cunha, "Laser-based trajectory tracking H2 control of autonomous rotorcraft," in *18th IFAC Symposium on Automatic Control in Aerospace*, September 2010.
- [17] —, "Lidar-based control of autonomous rotorcraft for inspection of pole-shaped structures," in *Second Iberian Robotics Conference (ROBOT'2015)*, vol. 417. Springer International, 2016, pp. 609–621.
- [18] I. Sa and P. Corke, *Vertical Infrastructure Inspection Using a Quadcopter and Shared Autonomy Control*. Berlin, Heidelberg: Springer Berlin Heidelberg, 2014, pp. 219–232.
- [19] I. Sa, S. Hrabar, and P. Corke, *Outdoor Flight Testing of a Pole Inspection UAV Incorporating High-speed Vision*. Cham: Springer International Publishing, 2015, pp. 107–121.
- [20] R. Mahony, V. Kumar, and P. Corke, "Multirotor aerial vehicles: Modeling, estimation, and control of quadrotor," *IEEE Robotics Automation Magazine*, vol. 19, no. 3, pp. 20–32, 2012.
- [21] M. Bangura and R. Mahony, "Nonlinear dynamic modeling for high performance control of a quadrotor," in *Australasian Conference on Robotics and Automation*, 2012.
- [22] G. D. Padfield, *Helicopter Flight Dynamics: The Theory and Application of Flying Qualities and Simulation Modeling*, ser. AIAA Education Series. Washington DC: AIAA, 1996.
- [23] R. Cunha, "Modeling and control of an autonomous robotic helicopter," Master's thesis, Department of Electrical and Computer Engineering, Instituto Superior Técnico, Lisbon, Portugal, May 2002.
- [24] D. Cabecinhas, R. Cunha, and C. Silvestre, "A nonlinear quadrotor trajectory tracking controller with disturbance rejection," *Control Engineering Practice*, vol. 26, pp. 1–10, 2014.
- [25] Asctec, "Pelican," 2015. [Online]. Available: <http://www.asctec.de/uav-uas-drohnen-flugsysteme/asctec-pelican/>
- [26] Mikrokopter, "Quadrox1," 2015. [Online]. Available: <http://www.mikrokopter.de/en/products/kits>
- [27] B. J. Guerreiro, C. Silvestre, R. Cunha, and D. Cabecinhas, "Lidar-based control of autonomous rotorcraft for the inspection of pier-like structures: Proofs," 2017. [Online]. Available: <https://arxiv.org/pdf/1705.01332.pdf>
- [28] C. Silvestre, "Multi-objective optimization theory with applications to the integrated design of controllers/plants for autonomous vehicles," Ph.D. dissertation, Instituto Superior Técnico, Universidade Técnica de Lisboa, Lisbon, Portugal, June 2000.
- [29] Vicon, "T-series," 2015. [Online]. Available: <http://www.vicon.com/products/camera-systems/t-series>
- [30] Pixhawk, "PX4FLOW," 2016. [Online]. Available: <https://pixhawk.org/modules/px4flow>